





Parametric study of the dispersion of inertial ellipsoidal particles in a wave-current flow

Laura K. C. Sunberg ¹, Michelle H. DiBenedetto ², Nicholas T. Ouellette ³,
and Jeffrey R. Koseff ³

¹*Institute of Arctic and Alpine Research, University of Colorado Boulder, Boulder, Colorado 80303, USA*

²*Department of Mechanical Engineering, University of Washington, Seattle, Washington 98115, USA*

³*The Bob and Norma Street Environmental Fluid Mechanics Laboratory, Department of Civil and Environmental Engineering, Stanford University, Stanford, California 94305, USA*



(Received 1 May 2023; accepted 25 January 2024; published 4 March 2024)

The degree to which particles such as larvae, seagrass pollen, and microplastics are dispersed by waves and currents influences many ecologically important aspects of their transport and fate. Particle transport models often assume dispersion is simply a function of the local turbulence, but there are many additional parameters related to both the particle characteristics and the flow dynamics that can impact how particles disperse. Here, we perform a parametric study of solutions to the Maxey-Riley equation and Euler's equation for rigid body motion for negatively buoyant, ellipsoidal particles dispersing in a wave-current flow. We systematically examine the impact of a comprehensive set of parameters on particle dispersion: the ratio between the time scales associated with particle settling and the waves, the Archimedes number, the particle eccentricity, the wave steepness, the Keulegan-Carpenter number, and the Stokes number. Our results show that no parameters can be discounted, but that the settling-wave time scale ratio has the largest influence on particle dispersion.

DOI: [10.1103/PhysRevFluids.9.034302](https://doi.org/10.1103/PhysRevFluids.9.034302)

I. INTRODUCTION

The extent to which particles are dispersed by ocean flows has many ecological consequences. These include effects related to natural particles, such as the retention rate of larvae in a region [1] and the level of genetic connectivity between different areas of seagrass [2], as well as to anthropogenic particles, such as the spread of microplastics from a river mouth [3]. Although they are small, particles such as larvae, seagrass pollen, and microplastics still have finite size and are not typically neutrally buoyant. As a result, they have some inertia of their own so that they do not simply follow the flow as tracers (e.g., Refs. [4,5]) and their physical characteristics as well as the flow dynamics impact how they disperse.

Particle properties that can impact dispersion include size, density, and shape. Particle size is known to modulate the dispersion of spheres in turbulence [6] and microplastics with different sizes distribute differently between the coastline and the open sea [7]. Many of the commonly found particles in the ocean (e.g., microplastics, seagrass pollen, and larvae) are typically nonspherical, which also complicates their transport and hence dispersion. Particle shape strongly influences particle transport in both quiescent fluids [8–11] and turbulent flows [12–16], and disks and rods have been shown to have dispersion values modulated by shape [17,18].

Waves are often a dominant flow feature in coastal areas and near the surface of the ocean. Models of particle transport sometimes include their effects by relating dispersion to wave-induced turbulence (e.g., Ref. [19]), but the unsteadiness of the waves themselves enhances particle dispersion even when the waves do not generate turbulence. Stokes drift [20,21] creates the opportunity for

Taylor dispersion [22,23] and variations in both the initial orientation of the particles and the initial phase of the waves can also lead to dispersion [24,25]. Recently, we performed an experimental study on the dispersion of nonspherical particles in a wave-current flow and found that particles dispersed up to four times as much in a current with waves as they did in a current alone [26]. The degree to which waves increased particle dispersion was a function of both particle shape and particle size. However, it was not feasible to discern the exact individual impacts of both particle shape and particle size experimentally, nor was it possible to explore the impact of each of the other relevant parameters on particle dispersion. We have also previously shown that the magnitude of the dispersion of ellipsoidal particles in a wavy flow is related to both particle shape and a ratio between the time scales associated with particle settling velocity and with waves, but the impact of these parameters was not disentangled from that of other varying parameters [24]. Other studies have likewise demonstrated the relevance of both particle and wave properties to particle distributions in the surf zone [27,28], but were also not able to explore the full parameter space.

Both particle properties and flow characteristics clearly matter to particle dispersion in a wavy flow. However, it is unclear what the individual contributions of each of these characteristics are. Therefore, we systematically examine the impact of a complete set of nondimensional parameters on particle dispersion using numerical simulations. We consider a nonturbulent wave-current system with sparsely distributed, finite-size, non-neutrally buoyant, ellipsoidal particles. A Buckingham Π analysis shows that this system can be fully described by six nondimensional parameters. We chose these parameters to be the settling-wave time scale ratio mentioned above, the Archimedes number, the particle eccentricity, the wave steepness, the Keulegan-Carpenter number, and the Stokes number. Our results show that the settling-wave time scale ratio causes the greatest range in dispersion, but that every parameter impacts dispersion in a nontrivial way. The relevance of each parameter highlights the complexity of the dynamics that determine dispersion. Models of large-scale transport of microplastics and other ocean particles often assume that dispersion rates are modified, if at all, only by the strength of the local turbulence [3,29,30]. Our results, however, show that parameters that describe wavy flow and particle characteristics are relevant to dispersion and can each lead to large ranges in dispersion values. Although the purpose of this study is to understand the effects of waves on particle dispersion and not to propose a new parametrization for particle dispersion, we note that our results imply that it is necessary for models to consider waves and particle characteristics in addition to turbulence in order to accurately predict particle transport.

II. METHODS

A. Nondimensional parameters

We consider negatively buoyant ellipsoidal particles dispersing in a wave-current flow. A Buckingham Π analysis shows that a set of six independent Π groups will fully describe the system because there are nine independent input variables (particle length scale d_s , particle eccentricity ϵ , particle density ρ_p , fluid density ρ_f , dynamic viscosity μ , gravity g , wave number k , wave amplitude A , and mean current velocity U) and three dimensions (length, time, and mass). We chose the Π groups to be the ratio between the settling time scale and the wave transport time scale $\frac{\tau_s}{\tau_w}$, the Archimedes number Ar , particle eccentricity ϵ , wave steepness kA , the Keulegan-Carpenter number KC , and the Stokes number St . The definitions of the Π groups are given below and also in Table I. To understand the variation in dispersion with these Π groups, we normalize the final standard deviation σ of the particles by $\frac{1}{k}$, as this is the only relevant horizontal length scale.

The ratio between the settling and wave transport time scales was shown to be helpful in understanding particle dispersion in wavy flow in [24], so we also include it here. It is defined as $\tau_s/\tau_w = [(L/w_p)]/[(L/u_s)] = u_s/w_p$, where L is the wavelength, u_s is the Stokes drift velocity $\omega k A^2$, and w_p is the particle settling velocity. We define w_p as $[gd_s^2(B-1)]/(18\nu\bar{K}')$, where \bar{K}' is the arithmetic mean of the eigenvalues of the resistance tensor K_{ij} and B is ρ_p/ρ_f . Note that [24] instead used a resistance value based on the preferential alignment of the particles; we do not do

TABLE I. Definitions of Π groups.

Π group	Mathematical definition	Physical meaning
τ_s/τ_w	$\frac{\omega k A^2}{[g d_s^2 (B-1)/(18\nu \bar{K}')]}$	Settling to wave time scale ratio
Ar	$\frac{g d_s^3 \rho_p (\rho_p - \rho_f)}{\mu^2}$	Gravity to viscosity force ratio
ϵ	$\frac{\lambda^2 - 1}{\lambda^2 + 1}$	Particle shape
kA	kA	Wave steepness
KC	$\frac{(\omega A + U)(1/\omega)}{d_s}$	Maximum fluid excursion length to particle length ratio
St	$\frac{k_T B d_s^2 / (18\nu)}{1/\omega}$	Particle response time to flow time scale ratio

this because the particles have competing wave- and settling-preferred orientations in our system. High values of τ_s/τ_w correspond to particles being transported by the waves for a long time prior to settling out and low values of τ_s/τ_w correspond to particles settling out of the waves quickly.

The Archimedes number Ar is defined as $Ar = [g d_s^3 \rho_p (\rho_p - \rho_f)]/\mu^2$. It represents the ratio between gravitational and viscous forces. We include it because it is reasonable that both gravitational and viscous forces would impact particle dispersion and because our previous experimental work indicated that dispersion varies with Ar [26].

We investigate the effects of particle shape through the particle eccentricity. The particle eccentricity is defined as $\epsilon = (\lambda^2 - 1)/(\lambda^2 + 1)$, where λ is the particle aspect ratio. The particle aspect ratio is defined as the ratio between the length along the axis of symmetry and the length along an orthogonal axis (see Fig. 1). So $\epsilon = -1$ corresponds to an infinitely thin disk, $\epsilon = 0$ corresponds to a sphere, and $\epsilon = 1$ corresponds to an infinitely thin rod.

The Keulegan-Carpenter number KC expresses the ratio between the maximum fluid excursion length and the particle length scale. We define it as $KC = (\omega A + |U|)(1/\omega)/d_s$. KC is the only Π group containing the current velocity U , so its variation is tied to variation in the current magnitude. A high value of KC corresponds to a current-dominated flow where particles are pushed through many wave orbitals at a rapid speed and a low value of KC corresponds to a wave-dominated flow. Holding KC constant between runs with variation in other Π groups keeps the distance traveled by a particle relative to the particle size constant across runs.

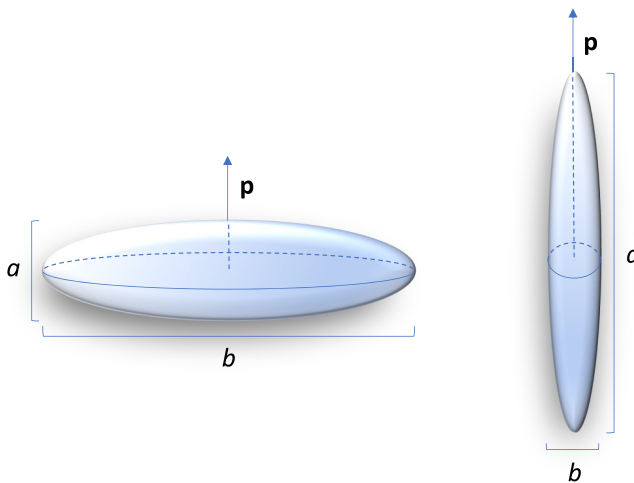


FIG. 1. Example oblate (left) and prolate (right) ellipsoids. The particle aspect ratio is defined as $\lambda = \frac{a}{b}$.

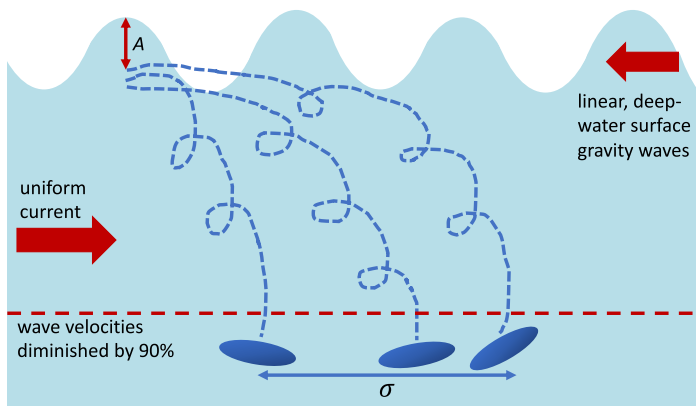


FIG. 2. Schematic of simulation. Particles were released one wave amplitude A below the surface of a wave-current flow with varied initial orientations and initial wave phase. The streamwise standard deviation of the particles was calculated once the particles had fallen to a depth where the wave velocities were diminished by 90%. Note that the particles remain submerged at all times; a trajectory appears to leave the fluid because the waves move in time.

The Stokes number St is defined as the ratio between the particle response time and the flow characteristic time scale. We define the flow characteristic time scale as $1/\omega$ and the particle response time as $(k_\tau B d_s^2)/(18\nu)$, where k_τ is a shape-dependent correction factor that accounts for the resistance equally in all directions [12,31]. This definition is an approximation because the true response time of nonspherical particles is a function of their orientation [16,24], but we still include the Stokes number in our Π set because it is so commonly used to describe particles in unsteady flows.

B. Simulation

We simulated negatively buoyant spheroidal ellipsoids released into a wave-current flow and measured their dispersion after they had fallen to a certain depth relative to the wave strength (see Fig. 2 for a schematic). The simulation was adapted from that used in [24], which simulates the motion of ellipsoidal particles using the Maxey-Riley equations and Euler's equation for rigid body motion. Full details about the simulation can be found in [24], so here we only describe the model in general and explain the adaptations we made to it—namely, including inertial torques in the rotational equations of motion and adding a current to the flow field.

The spatial trajectories of the particles were computed using the Maxey-Riley equation [32]. The Maxey-Riley equation assumes a Stokes number much less than one. We neglect the Basset history forces because the particles are settling and traveling with the current, so they should interact very little with their own wakes. We also neglect Saffman lift forces because they scale with $\frac{d_s^2}{\nu} \frac{U_0}{L}$, which remains less than 0.1 for disks and less than 1 for spheres and rods in the cases we examined. Here, d_s is the diameter of a volume-equivalent sphere, ν is the kinematic viscosity of the fluid, and $\frac{U_0}{L}$ is the scale of the velocity gradients in the undisturbed flow, which is $\omega A k$, where ω is the wave frequency, A is the wave amplitude, and k is the wave number. Additionally, particle-particle interactions are not included because the particles are sparsely distributed in the applications we are considering.

To adapt the Maxey-Riley equation for ellipsoidal particles, the added mass term is implemented with a shape-dependent tensor of added mass coefficients C_{ij}^m [33–35] and the drag term is implemented with a shape-dependent resistance tensor K_{ij} [36–38]. The version of the Maxey-Riley

equation used in the simulation is therefore

$$\frac{dv_i}{dt} = \frac{1}{B} \frac{Du_i}{Dt} - \frac{1}{B} C_{ij}^m \frac{d}{dt} (v_j - u_j) - 18 \frac{\nu}{Bd_s^2} K_{ij} (v_j - u_j) - \left(1 - \frac{1}{B}\right) g \delta_{i3}, \quad (1)$$

where B is the ratio between the particle density and the fluid density and g is the acceleration due to gravity.

The simulation calculates the orientations of the particles using Euler's equation for rigid body motion in the body-axis frame of the particle, namely

$$I_{ij} \frac{d\omega_j}{dt} + \epsilon_{ijk} \omega_j I_{kl} \omega_l = M_i^J + M_i^I, \quad (2)$$

where I_{ij} is the particle moment of inertia tensor, ω_i is the rate of angular rotation of the particle, ϵ_{ijk} is the Levi-Civita symbol, M_i^J represents the Jeffery torques [39], and M_i^I represents the inertial torques, which were an addition to the simulation for this study. The inertial torque is computed as

$$M_i^I = F(\lambda) \rho_f |v_j - u_j|^2 d_{\max}^3 p_j (\widehat{v_j - u_j}) \epsilon_{ilm} p_l (\widehat{v_m - u_m}), \quad (3)$$

where $F(\lambda)$ is a shape factor (Eqs. 4.1 and 4.2 in [40]), ρ_f is the density of the fluid, d_{\max} is the maximum length dimension of the particle, \mathbf{p} is a unit vector pointing along the particle's axis of symmetry (Fig. 1), and the hat ($\widehat{}$) indicates that a vector has been normalized by its magnitude [41,42]. Due to the inertial torques, particles simulated in quiescent fluid orient with their broad side facing down, such that their drag coefficient is maximized, as expected from prior literature [41,43]. They reach this preferred orientation more quickly when they are more inertial.

We simulate a flow field similar to that from our previous experiment on particle dispersion [26], with linear, deep-water surface gravity waves opposed by a nonturbulent current. The current is uniform and the flow (unlike in the experiment) is infinitely deep. Wave-current interactions are not included. We assume that the particles do not affect the flow. The flow is given by

$$\mathbf{u}(x, z, t) = \omega A e^{kz} [\cos(kx - \omega t) \hat{\mathbf{e}}_x + \sin(kx - \omega t) \hat{\mathbf{e}}_z] - U \mathbf{e}_x, \quad (4)$$

where k is the wave number and U is the current magnitude. We define ω using the deep-water approximation for the dispersion relation: $\omega = \sqrt{gk}$.

To vary the Π groups independently and systematically, we chose a desired set of Π group values and then set the values of the dimensional parameters in the equations of motion accordingly, using MATLAB's symbolic solver to find the value of each of the dimensional parameters as a function of the Π groups. For each set of Π values, we performed 200 realizations of an individual ellipsoid falling in a wave-current flow. The initial orientation of the particle in each realization was selected from a uniform distribution of points on a unit sphere and each particle was released at a wave phase selected from a uniform distribution. The variation in the particles' initial conditions meant that they all followed different orientational and spatial trajectories, allowing for dispersion. The particles were released at a depth A below the instantaneous free surface with an initial velocity equal to the sum of the local flow velocity and the terminal settling velocity of a volume-equivalent sphere. Because the waves are deep-water waves and the particles are negatively buoyant, the particles fall out of the wave-influenced flow region over time. We ran the simulations until the mean vertical position of all of the particles reached a depth where the waves were reduced to 10% of their surface magnitude (i.e., until the mean depth of the particles was $\frac{1}{k} \ln 0.1 \approx 0.37L$, where L is the wavelength). We then took the streamwise standard deviation σ of the particle locations to measure the dispersion, as particles primarily dispersed along the streamwise axis. Error bars on the standard deviations were calculated with bootstrapping [44].

Figure 3 demonstrates how individual particle orientations and particle group dispersion develop over time t (normalized by wave period T) for two example cases. Subplots (a) and (c) correspond to a case of disks with nondimensional parameters set to the values used in the base case (referred to as Example Case 1). Subplots (b) and (d) correspond to a case where disks reorient more slowly relative to the speed with which they fall out of the waves (referred to as Example Case 2). After being

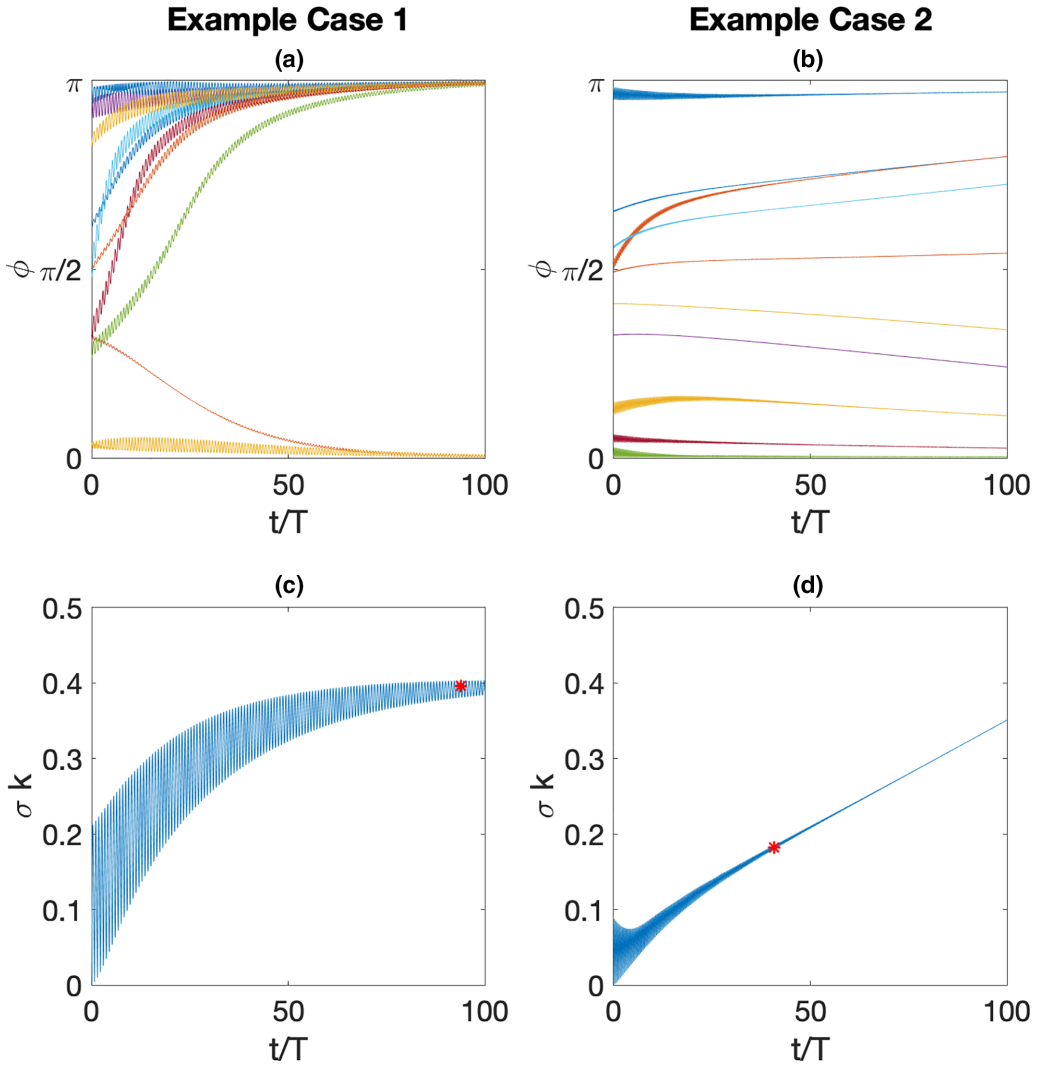


FIG. 3. Subplots (a) and (b) show the variation in the angle, ϕ , between the axis of symmetry of particles and gravity over time t normalized by the period length T , with each curve corresponding to the orientational trajectory of a specific particle. Subplots (c) and (d) show how the streamwise standard deviation of a full set of particles σ normalized by $1/k$ varies over nondimensionalized time t/T . The red asterisks in subplots (c) and (d) denote the time when the particles reach the cutoff depth of $0.37L$. Subplots (a) and (c) correspond to Example Case 1, where the nondimensional parameters are set to the base case, and subplots (b) and (d) correspond to Example Case 2, where particles align more slowly than in the base case.

released with randomly varied initial conditions, each of the particles takes a different orientational trajectory [subplots (a) and (b)]. In both example cases, the waves cause the particles to rock back and forth at the period of the waves (oscillations in the orientational trajectories). In Example Case 1, the disks align over time to settle with their broad side facing down, i.e., an orientation of $\phi = 0$ or $\phi = \pi$, where ϕ is the angle between the axis of symmetry of the particle and gravity [subplot (a)]. In Example Case 2, the particles align more slowly and do not reach a preferential alignment prior to falling out of the waves [subplot (b)].

Subplots (c) and (d) show the change over time of the streamwise standard deviations of the particles σ normalized by $1/k$. The dispersion oscillates over time as the particles are pushed towards and apart from each other by the wave orbitals. These oscillations weaken as the particles fall out of the waves. In Example Case 1, dispersion asymptotes to roughly 0.4 as the particles reach their preferential alignment and fall out of the waves [subplot (c)]. In Example Case 2, the particles only reorient very slowly after they have fallen out of the waves and their varied orientations continue to provide a dispersion mechanism long after the waves have ceased to provide a direct dispersion mechanism [subplot (d)]. The red asterisks in subplots (c) and (d) show the time when the particles reach a depth of $0.37L$, which is where dispersion is measured in all subsequent simulation runs. The depth cutoff allows us to focus on the effects of waves on dispersion rather than on dispersion increases due to particle misalignment alone after the particles are no longer in the waves.

III. RESULTS AND DISCUSSION

In our base case, the Π groups had values of $\tau_s/\tau_w = 10$, $Ar = 20$, $\epsilon = -0.9$ (oblate), $kA = 0.2$, $St = 0.05$, and $KC = 500$. These values were chosen because they were associated with relatively high dispersion, signifying that none of the parameters had been pushed to a regime where they overwhelmed dispersion induced by other parameters. For reference for readers accustomed to working with the particle Reynolds number, these base case values correspond to a particle Reynolds number $Re_p = d_s w_p / \nu$ of 0.6. To explore the impact of each Π group on particle dispersion, we systematically varied two Π groups at a time while holding the other Π groups' values fixed at their base case values. In the sets of plots that follow, the horizontal axis shows the range of one Π group, while the different curves correspond to different values of the second Π group. In each set of plots, the subplot that would have the same Π group both defining the horizontal axis and the different curve values is omitted. Because we normalize dispersion by $1/k$, it is not reasonable to show plots against kA , but we can generally state that larger values of kA lead to enhanced dispersion.

Figure 4 shows nondimensional dispersion plotted against the settling-wave time scale ratio τ_s/τ_w . Variation in τ_s/τ_w led to the largest range of dispersion values out of all of the Π groups in the set. The maximum range of dispersion values caused by variation in τ_s/τ_w was 1 (in dimensionless units), while no other nondimensional parameter led to a range in dispersion values greater than 0.2. Higher values of τ_s/τ_w correspond to higher values of dispersion, which is expected because the particles have more time to have their orientations and positions scrambled by the waves when τ_s/τ_w is large. The increase in dispersion with τ_s/τ_w is in agreement with the results of [24] and, although the magnitude of the increase may vary slightly with different values of other parameters, the same trend can be seen in every subplot. We note that, for intermediate and high values of τ_s/τ_w , the particles align with their broad side down by the time they fall out of the waves, while the initial orientations of particles with low values of τ_s/τ_w persist. The variability in the orientations of particles with low τ_s/τ_w at depth means that if the simulation were run longer dispersion would continue to increase without bound for these cases (as discussed earlier with respect to Fig. 3).

Although the settling-wave time scale ratio leads to the greatest range in dispersion values, each of the other parameters can lead to small variations in dispersion and the impacts of each of the parameters are interconnected. Figure 5 shows nondimensional dispersion plotted against the Archimedes number Ar . The maximum range of the dispersion with Ar is 0.2, which, although much smaller than the range associated with τ_s/τ_w , corresponds to dispersion tripling between $Ar = 5$ and $Ar = 40$ for rods and spheres [subplot (c)]. For all of the curves except those associated with low values of τ_s/τ_w in subplot (a) and those associated with $\epsilon = 0$ and $\epsilon = 0.9$ in subplot (c), the value of dispersion initially increases with increasing Ar and then decreases for higher values of Ar . This variation in dispersion with Ar is what one might expect: in the low Ar limit, the particles are more like flow tracers and therefore disperse less. When Ar is high, gravitational forces dominate so the particle is less impacted by the waves. At intermediate Ar , the particle experiences high enough gravitational forces so that they do not follow the flow, but not so high that they simply plummet

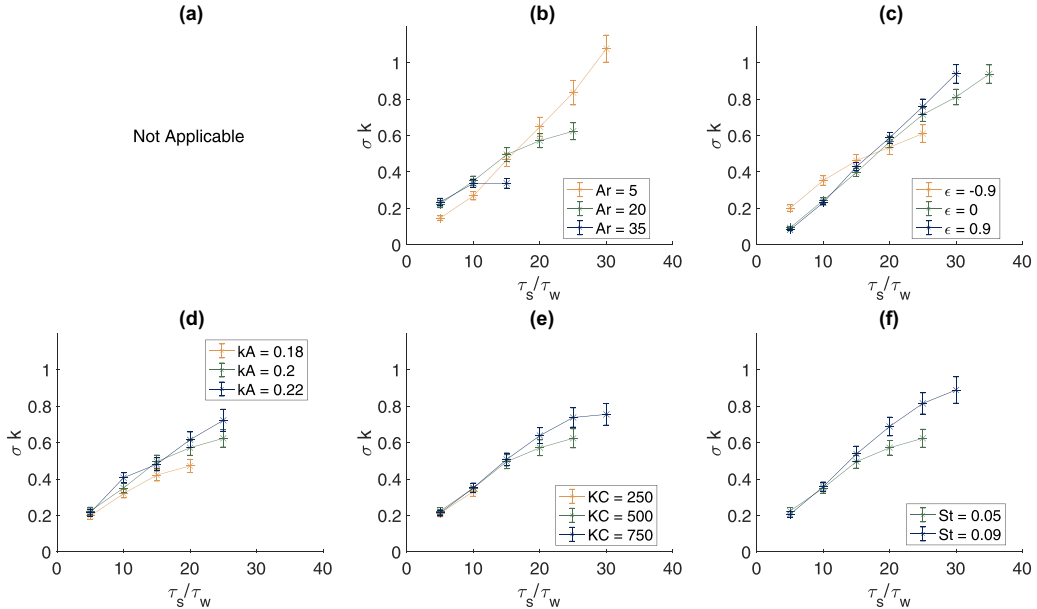


FIG. 4. Streamwise standard deviation of the particles normalized by $1/k$ plotted against the settling-wave time scale ratio τ_s/τ_w . Different curves correspond to different values of the other Π groups. Error bars show 95% confidence intervals computed with bootstrapping. Subplot (a) is omitted; see text.

without being affected by the waves. Low values of τ_s/τ_w [subplot (a)] do not allow for high enough dispersion for this trend to be seen, which further highlights the importance of τ_s/τ_w in determining dispersion. Rods and spheres [subplot (c)] are associated with lower dispersion for low values of Ar than any of the disk cases but with higher dispersion for higher Ar .

Figure 6 shows dispersion plotted against particle eccentricity ϵ . When shape mattered at all, oblate particles (lower eccentricity) were associated with higher dispersion. In these cases, oblate particles tended to align more slowly and “rock” (oscillate orientationally at the period of the waves) more as they aligned, which enhanced their dispersion. Higher values of τ_s/τ_w [subplot (a)] or Ar [subplot (b)] or lower values of kA [subplot (d)] or KC [subplot (e)] could cause them to align more quickly and/or rock less.

Dispersion is plotted against the Keulegan-Carpenter number KC in Fig. 7. Higher values of KC correspond to a higher current and the particles being “pushed” through the waves more quickly. There is somewhat less variation in dispersion with KC than with Ar or ϵ and it is difficult to identify any trends for most of the cases. Because particles are quickly pushed through the wave field at high values of KC , the way they trace out wave orbitals is not as likely to generate dispersion. However, the particles can still disperse if the waviness of the flow leads to variation in their orientations. Most of the cases plotted are for disks with at least intermediate values of Ar . These rock easily in response to small perturbations and so disperse even at high values of KC . However, for low values of Ar [subplot (b)] and for spheres and rods [subplot (c)], increasing KC generally corresponds to decreasing dispersion. Spheres are symmetric and therefore the dynamics are not affected if they reorient and rods preferentially orient perpendicular to the flow at high values of KC , so they do not rock easily. Lower values of Ar correspond to tracerlike particles, which also tend to rock less. Therefore, in these three cases the particles disperse less at high values of KC .

Dispersion is plotted against the Stokes number St in Fig. 8. In order to satisfy our assumptions for the simulation, St must be small, so we could not explore a large range of St numbers. Therefore,

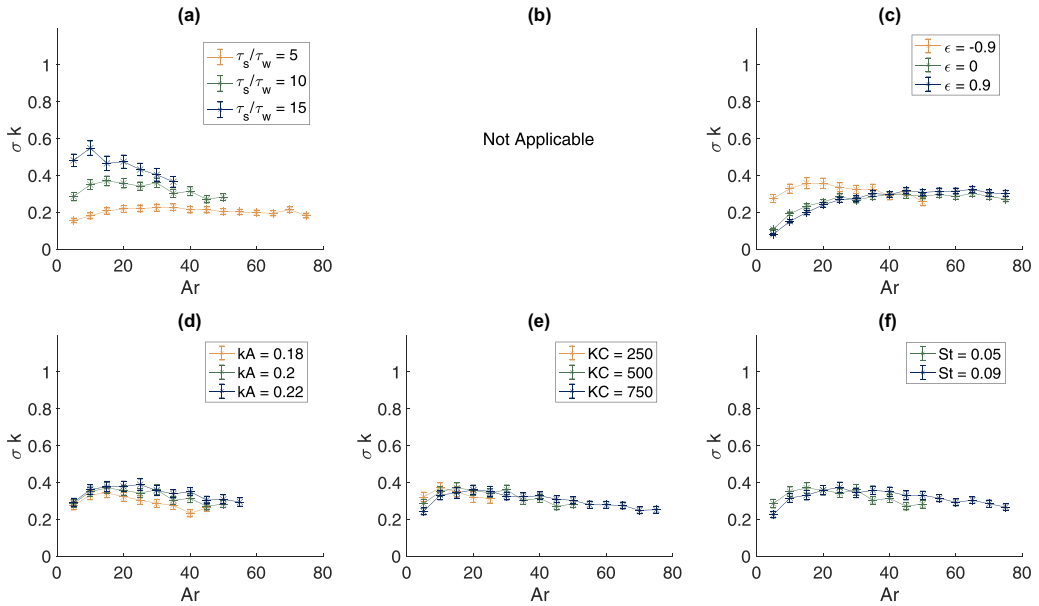


FIG. 5. Streamwise standard deviation of the particles normalized by $1/k$ plotted against the Archimedes number Ar . Subplot (b) is omitted; see text.

there is limited variation with St , although it is likely that dispersion would vary more with St over a larger range of St values. Arguably, when τ_s/τ_w [subplot (a)] is large, dispersion increases with increasing St . For low Ar [subplot (b)] and disks and rods [subplot (c)], higher values of St are

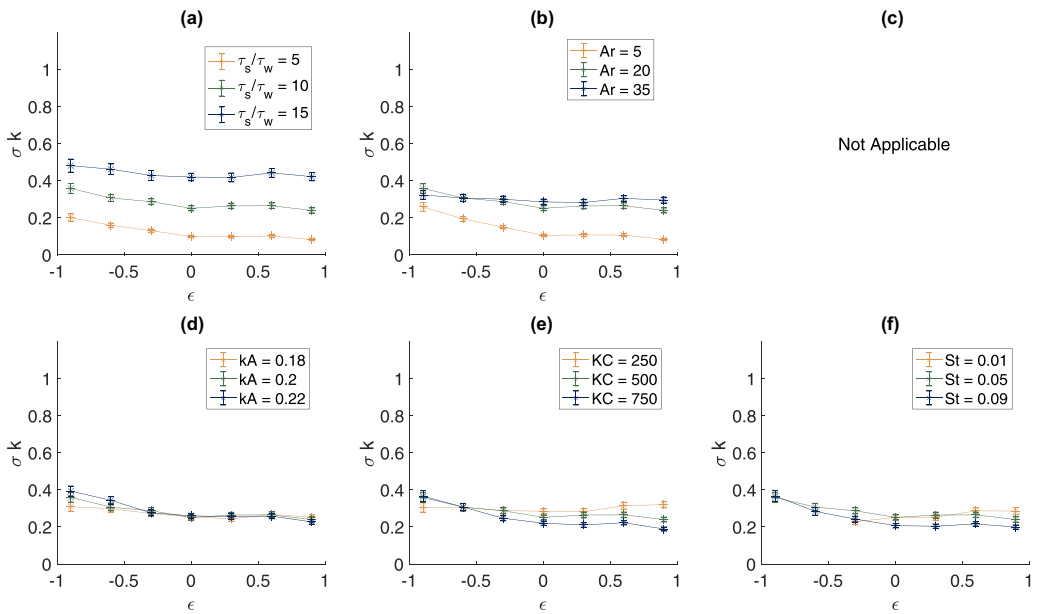


FIG. 6. Streamwise standard deviation of the particles normalized by $1/k$ plotted against particle eccentricity ϵ . Subplot (c) is omitted; see text.

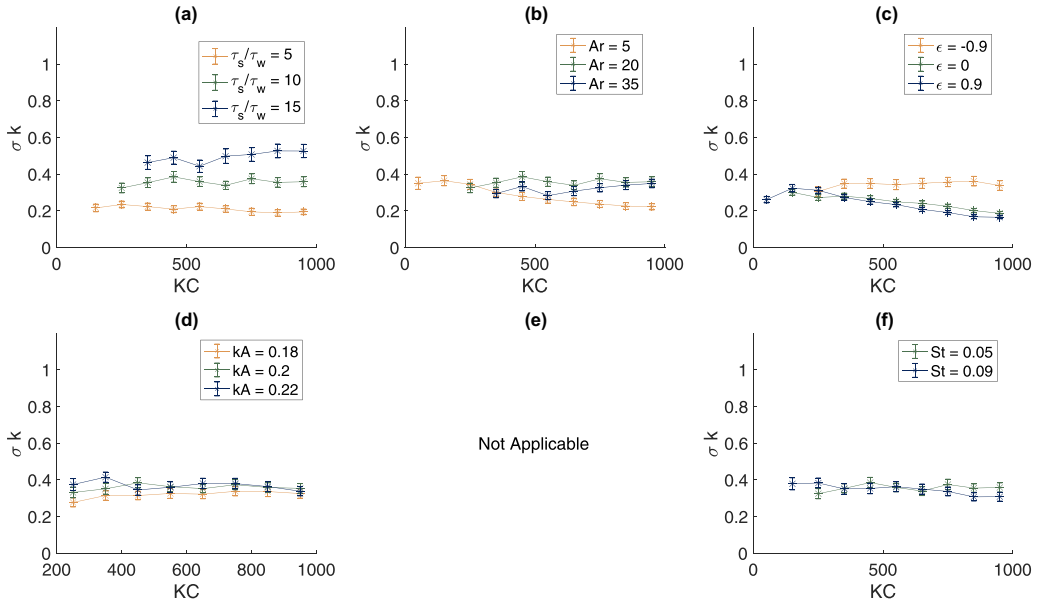


FIG. 7. Streamwise standard deviation of the particles normalized by $1/k$ plotted against the Keulegan-Carpenter number KC . Subplot (e) is omitted; see text.

associated with lower dispersion. Dispersion does not vary with St for any of the values of kA [subplot (d)] or KC [subplot (d)] tested when the other parameters have values associated with the base case.

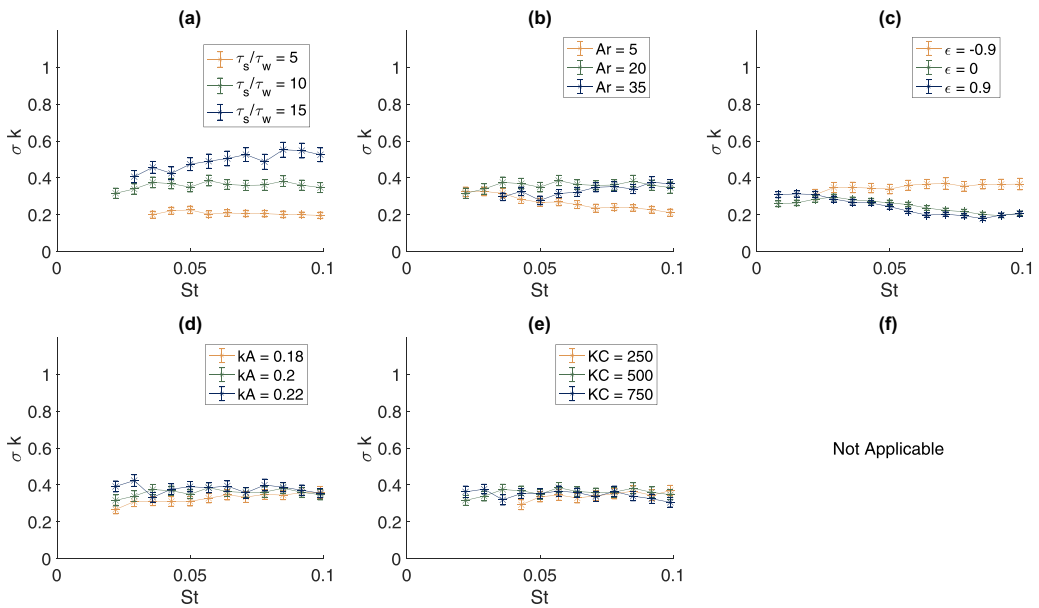


FIG. 8. Streamwise standard deviation of the particles normalized by $1/k$ plotted against the Stokes number St . Subplot (f) is omitted; see text.

IV. CONCLUSION

In summary, we found that the settling-wave time scale ratio causes the largest range of dispersion values within our chosen set of nondimensional numbers. High values of the settling-wave time scale ratio are associated with enhanced dispersion because the particles remain in the waves longer so that the waves have greater opportunity to disperse them. When models of particle transport incorporate wave effects, they typically only include dispersion due to wave-induced turbulence [19]. The large range of dispersion values associated with the settling-wave time scale ratio shows that the unsteadiness introduced by the waves can also lead to significant dispersion. While the settling-wave time scale ratio leads to the greatest range in dispersion values, all of the other parameters we examined impact dispersion as well, often in interrelated ways. These results highlight the richness of the dynamics of nonspherical particles settling in a wavy flow and indicate the importance of accounting for both the flow and particle parameters in order to accurately predict particle transport in coastal flows.

ACKNOWLEDGMENTS

L.K.C.S. acknowledges support from ARCS Foundation. We would also like to thank Stanford University and the Stanford Research Computing Center for providing computational resources and support through the Sherlock cluster.

-
- [1] B. Daly, C. Parada, T. Loher, S. Hinckley, A. J. Hermann, and D. Armstrong, Red king crab larval advection in bristol bay: Implications for recruitment variability, *Fish. Oceanogr.* **29**, 505 (2020).
 - [2] G. A. Kendrick, M. Waycott, T. J. Carruthers, M. L. Cambridge, R. Hovey, S. L. Krauss, P. S. Lavery, D. H. Les, R. J. Lowe, O. M. I. Vidal *et al.*, The central role of dispersal in the maintenance and persistence of seagrass populations, *Bioscience* **62**, 56 (2012).
 - [3] E. van Sebille, S. Aliani, K. L. Law, N. Maximenko, J. M. Alsina, A. Bagaev, M. Bergmann, B. Chapron, I. Chubarenko, A. Cózar *et al.*, The physical oceanography of the transport of floating marine debris, *Environ. Res. Lett.* **15**, 023003 (2020).
 - [4] W. S. Arnold, G. L. Hitchcock, M. E. Frischer, R. Wanninkhof, and Y. Peter Sheng, Dispersal of an introduced larval cohort in a coastal lagoon, *Limnol. Oceanogr.* **50**, 587 (2005).
 - [5] A. de Vos, L. Aluwihare, S. Youngs, M. H. DiBenedetto, C. P. Ward, A. P. Michel, B. C. Colson, M. G. Mazzotta, A. N. Walsh, R. K. Nelson *et al.*, The M/V X-press Pearl nurdle spill: Contamination of burnt plastic and unburnt nurdles along Sri Lanka's beaches, *ACS Environ. Au* **2**, 128 (2022).
 - [6] M. Bouvard and S. Petkovic, Vertical dispersion of spherical, heavy particles in turbulent open channel flow, *J. Hydraul. Res.* **23**, 5 (1985).
 - [7] V. Onink, M. L. Kaandorp, E. van Sebille, and C. Laufkötter, Influence of particle size and fragmentation on large-scale microplastic transport in the Mediterranean Sea, *Environ. Sci. Technol.* **56**, 15528 (2022).
 - [8] W. W. Willmarth, N. E. Hawk, and R. L. Harvey, Steady and unsteady motions and wakes of freely falling disks, *Phys. Fluids* **7**, 197 (1964).
 - [9] F. Auguste, J. Magnaudet, and D. Fabre, Falling styles of disks, *J. Fluid Mech.* **719**, 388 (2013).
 - [10] F. Candelier and B. Mehlig, Settling of an asymmetric dumbbell in a quiescent fluid, *J. Fluid Mech.* **802**, 174 (2016).
 - [11] J. B. Will, V. Mathai, S. G. Huisman, D. Lohse, C. Sun, and D. Krug, Kinematics and dynamics of freely rising spheroids at high Reynolds numbers, *J. Fluid Mech.* **912**, A16 (2021).
 - [12] F. Zhao, W. K. George, and B. G. M. Van Wachem, Four-way coupled simulations of small particles in turbulent channel flow: The effects of particle shape and Stokes number, *Phys. Fluids* **27**, 083301 (2015).
 - [13] G. A. Voth and A. Soldati, Anisotropic particles in turbulence, *Annu. Rev. Fluid Mech.* **49**, 249 (2017).

- [14] N. Pujara and E. A. Variano, Rotations of small, inertialess triaxial ellipsoids in isotropic turbulence, *J. Fluid Mech.* **821**, 517 (2017).
- [15] T. B. Oehmke, A. D. Bordoloi, E. Variano, and G. Verhille, Spinning and tumbling of long fibers in isotropic turbulence, *Phys. Rev. Fluids* **6**, 044610 (2021).
- [16] L. J. Baker and F. Coletti, Experimental investigation of inertial fibres and disks in a turbulent boundary layer, *J. Fluid Mech.* **943**, A27 (2022).
- [17] L. Esteban, J. Shrimpton, and B. Ganapathisubramani, Disks settling in turbulence, *J. Fluid Mech.* **883**, A58 (2020).
- [18] M. Shin and D. L. Koch, Rotational and translational dispersion of fibres in isotropic turbulent flows, *J. Fluid Mech.* **540**, 143 (2005).
- [19] T. X. Thoman, T. Kukulka, and K. Gamble, Dispersion of buoyant and sinking particles in a simulated wind- and wave-driven turbulent coastal ocean, *J. Geophys. Res.: Oceans* **126**, e2020JC016868 (2021).
- [20] G. G. Stokes, On the theory of oscillatory waves, *Trans. Cambridge Philos. Soc.* **8**, 441 (1847).
- [21] I. Eames, Settling of particles beneath water waves, *J. Phys. Oceanogr.* **38**, 2846 (2008).
- [22] A. W. K. Law, Taylor dispersion of contaminants due to surface waves, *J. Hydraul. Res.* **38**, 41 (2000).
- [23] J. Pearson, I. Guymer, J. West, and L. Coates, Effect of wave height on cross-shore solute mixing, *J. Waterway, Port, Coastal, Ocean Eng.* **128**, 10 (2002).
- [24] M. H. DiBenedetto, N. T. Ouellette, and J. R. Koseff, Transport of anisotropic particles under waves, *J. Fluid Mech.* **837**, 320 (2018).
- [25] M. H. DiBenedetto, L. K. Clark, and N. Pujara, Enhanced settling and dispersion of inertial particles in surface waves, *J. Fluid Mech.* **936**, A38 (2022).
- [26] L. K. Clark, M. H. DiBenedetto, N. T. Ouellette, and J. R. Koseff, Dispersion of finite-size, non-spherical particles by waves and currents, *J. Fluid Mech.* **954**, A3 (2023).
- [27] P. L. Forsberg, D. Sous, A. Stocchino, and R. Chemin, Behaviour of plastic litter in nearshore waters: First insights from wind and wave laboratory experiments, *Mar. Pollut. Bull.* **153**, 111023 (2020).
- [28] N. B. Kerpen, T. Schlurmann, A. Schendel, J. Gundlach, D. Marquard, and M. Hüpgen, Wave-induced distribution of microplastic in the surf zone, *Front. Mar. Sci.* **7**, 590565 (2020).
- [29] T. Kukulka and K. Brunner, Passive buoyant tracers in the ocean surface boundary layer: 1. Influence of equilibrium wind-waves on vertical distributions, *J. Geophys. Res.: Oceans* **120**, 3837 (2015).
- [30] K. Brunner, T. Kukulka, G. Proskurowski, and K. L. Law, Passive buoyant tracers in the ocean surface boundary layer: 2. Observations and simulations of microplastic marine debris, *J. Geophys. Res.: Oceans* **120**, 7559 (2015).
- [31] M. Shapiro and M. Goldenberg, Deposition of glass fiber particles from turbulent air flow in a pipe, *J. Aerosol Sci.* **24**, 65 (1993).
- [32] M. R. Maxey and J. J. Riley, Equation of motion for a small rigid sphere in a nonuniform flow, *Phys. Fluids* **26**, 883 (1983).
- [33] H. Lamb, *Hydrodynamics* (Dover Publications, New York, 1945), pp. 153–154.
- [34] I. Gallily and A.-H. Cohen, On the orderly nature of the motion of nonspherical aerosol particles. II. inertial collision between a spherical large droplet and an axially symmetrical elongated particle, *J. Colloid Interface Sci.* **68**, 338 (1979).
- [35] C. Siewert, R. Kunnen, M. Meinke, and W. Schröder, Orientation statistics and settling velocity of ellipsoids in decaying turbulence, *Atmos. Res.* **142**, 45 (2014).
- [36] A. Oberbeck, Ueber stationäre flüssigkeitsbewegungen mit berücksichtigung der inneren reibung, *J. Reine Angew. Math.* (1876).
- [37] H. Brenner, The stokes resistance of an arbitrary particle—II: An extension, *Chem. Eng. Sci.* **19**, 599 (1964).
- [38] E. Loth, Drag of non-spherical solid particles of regular and irregular shape, *Powder Technol.* **182**, 342 (2008).
- [39] G. B. Jeffery, The motion of ellipsoidal particles immersed in a viscous fluid, *Proc. R. Soc. London Ser. A* **102**, 161 (1922).
- [40] V. Dabade, N. K. Marath, and G. Subramanian, Effects of inertia and viscoelasticity on sedimenting anisotropic particles, *J. Fluid Mech.* **778**, 133 (2015).

- [41] K. Gustavsson, M. Sheikh, A. Naso, A. Pumir, and B. Mehlig, Effect of particle inertia on the alignment of small ice crystals in turbulent clouds, *J. Atmos. Sci.* **78**, 2573 (2021).
- [42] F. Jiang, L. Zhao, H. I. Andersson, K. Gustavsson, A. Pumir, and B. Mehlig, Inertial torque on a small spheroid in a stationary uniform flow, *Phys. Rev. Fluids* **6**, 024302 (2021).
- [43] A. Hazzab, A. Terfous, and A. Ghenaim, Measurement and modeling of the settling velocity of isometric particles, *Powder Technol.* **184**, 105 (2008).
- [44] B. Efron and R. Tibshirani, Bootstrap methods for standard errors, confidence intervals, and other measures of statistical accuracy, *Statist. Sci.* **1**, 54 (1986).